AIAA 2003–3282

Jet Noise Prediction Using Stochastic Turbulence Modeling

Mattias Billson*, Lars-Erik Eriksson*† and Lars Davidson*

* *Department of Thermo and Fluid Dynamics, Chalmers University of Technology, SE-412 96 Göteborg, Sweden*

† *Volvo Aero Corporation, Military Engines Division, SE-461 81 Trollhättan, Sweden*

9th AIAA/CEAS Aeroacoustic Conference may 12–14, 2003/Hilton Head, South Carolina

Jet Noise Prediction Using Stochastic Turbulence Modeling

Mattias Billson*, Lars-Erik Eriksson*† and Lars Davidson*
* *Department of Thermo and Fluid Dynamics, Chalmers University of Technology, SE-412 96 Göteborg, Sweden*
† *Volvo Aero Corporation, Military Engines Division, SE-461 81 Trollhättan, Sweden*

This work is an attempt to capture the sound field of a high Reynolds number, high Mach number subsonic jet without LES or DNS. The method used is called the SNGR (Stochastic Noise Generation and Radiation) method and was first proposed by Bechara, Bailly, Lafon Candel and Juvé.[1,2] The SNGR method is based on using the information given from a RANS solution to generate a time dependent velocity source field which is used to evaluate source terms for the linearized Euler equations. The solution to the linearized Euler equations provide the acoustic information of the flow.

This method has in the present work been further developed with a new time dependence and convection of the generated velocity field.

The developed method has been applied to a Mach 0.75 cold jet at $\mathrm{Re} = DU_j/\nu = 750,000$ and compared to recent LES computations and measurements of the same jet.

Introduction

An aeroacoustic problem can be divided into generation of sound and propagation of the generated sound. Solving the full compressible Navier-Stokes equations using LES or DNS captures both. The computational cost however of the two methods prohibits the use of them for most industrial applications.

There has recently been some progress in a new modeling approach called SNGR[1,2] (Stochastic Noise Generation and Radiation) model. It is based on the idea that the linearized Euler equations are a wave operator for acoustic perturbations. Introducing suitable sources to the linearized Euler equations result in accurate predictions of the generation and propagation of acoustic perturbations. The objective is that this approach will cost less computationally than performing a LES, especially at high Reynolds numbers.

In the SNGR method a RANS solution provides time averaged information about the flow field. The challenge is then to use the information given from the RANS solution to generate an instationary turbulent velocity field with the same local statistical properties as the RANS solution. This generated turbulent field is used for evaluation source terms in the linearized Euler equations. Solving the linearized Euler equations with the source terms provide the propagation of sound from the source region to the far-field.

The present paper is organized as follows. The role of the RANS solution is briefly discussed in the following section followed by the presentation of the derived source terms for the linearized Euler equations. The basic concept of how the synthesized turbulence is generated is desribed and then the differences between the present method and the ones proposed in Refs. (1, 2) are discussed. The differences concern how time dependence and convection is introduced in the generation of the synthesized turbulence.

Comparison of the synthesized turbulence with theory for isentropic turbulence will first be presented. Next a simulation of a 3D jet is presented beginning with the computational setup and followed by the results which are compared to both measurements, Jordan and Gervais[3,4] and recent Large Eddy Simulations, Andersson *et al.*[5] Differences between the measurements and the present simulations are then investigated and this is followed by the conclusions.

The SNGR method

The SNGR model is performed in three steps. These are:

step 1. A Reynolds-Averaged Navier-Stokes solution of a compressible turbulent jet is calculated using, for example, a $k-\varepsilon$ turbulence model.

step 2. An instationary turbulent velocity field with the same local turbulence kinetic energy, time scale and length scale as the RANS solution is generated using random Fourier modes.

step 3. The linearized Euler equations are solved using the mean flow field computed in step (1)

as mean flow solution. Source terms derived in a similar way as for Lighthill's wave equation are evaluated using the turbulent field generated in step (2). The linearized Euler equations then gives the propagation of sound from the turbulent field to the surrounding far-field.

RANS for Jet Computations

The Reynolds-Averaged Navier-Stokes solution (RANS) of the flow field is computed using a standard $k-\varepsilon$ turbulence model. The purpose of the RANS solution is to provide a mean flow solution for the linearized Euler computation. The RANS solution is also used in the stochastic modeling of the turbulent field. The SNGR model needs input parameters in the form of turbulence kinetic energy, length scale and time scale. The turbulence kinetic energy is one of the solution variables from the RANS computation and the turbulence length scale and time scale are computed from the turbulence kinetic energy and the turbulence dissipation rate. For more details, see Billson.[6]

Linearized Euler Equations with Source Terms

A formal derivation of the source terms for the linearized Euler equations is given in Billson.[7] Given here is only the final set of equations.

$$
\begin{aligned}
\frac{\partial \rho'}{\partial t} + \frac{\partial (\rho u_j)'}{\partial x_j} &= 0 \\
\frac{\partial (\rho u_i)'}{\partial t} + \frac{\partial}{\partial x_j}(\widetilde{u}_j(\rho u_i)' + \widetilde{u}_i(\rho u_j)' - \rho'\widetilde{u}_i\widetilde{u}_j + p'\delta_{ij}) &= \\
-\frac{\partial}{\partial x_j}(\rho u_i'' u_j'' - \overline{\rho u_i'' u_j''}) & \\
\frac{\partial (\rho e_0)'}{\partial t} + \frac{\partial}{\partial x_j}(\widetilde{h}_0(\rho u_j)' + \widetilde{u}_j(\rho h_0)' - \rho'\widetilde{h}_0\widetilde{u}_j) &= \\
-\frac{\partial}{\partial x_j}(\rho h_0'' u_j'' - \overline{\rho h_0'' u_j''}) &
\end{aligned}
\tag{1}
$$

The left-hand side of equations 1 is the linearized Euler equations. The right-hand side contains all non-linearities that emerged when the Euler equations were rewritten into the linearized Euler equations. Thus, equations 1 are still the full non-linear Euler equations. If the right-hand side of the equations is treated as a source and is in some way known, then the left-hand side is a wave operator responding to the source.

A validation of the derived source terms has been performed in the case of a forced 2D mixing layer in Billson[6] where the solution of the linearized Euler equations with the derived source terms was compared to a direct simulation of the same flow. The source terms were shown to be working well and given that they are evaluated from a physical solution, the response from the linearized Euler equations is in good agreement with the direct numerical simulation used to evaluate the source terms.

Stochastic Modeling of Turbulence

This section concerns the generation of an instationary turbulent velocity field, i.e. Step (2) in the SNGR method. A time-space turbulent velocity field can be simulated using random Fourier modes. This was proposed by Kraichnan[8] and Karweit *et al.*[9] and further developed by Bechara *et al.*[1] and Bailly and Juvé.[2] The velocity field is then given by

$$
\mathbf{u}_t(\mathbf{x}) = 2\sum_{n=1}^{N} \hat{u}_n \cos(\mathbf{k}_n \mathbf{x} + \psi_n)\sigma_n \tag{2}
$$

where $\hat{u}_n$, ψ_n and σ_n are amplitude, phase and direction of the n^{th} Fourier mode. Figure 1 shows the geometry of the n^{th} mode in wave number space.

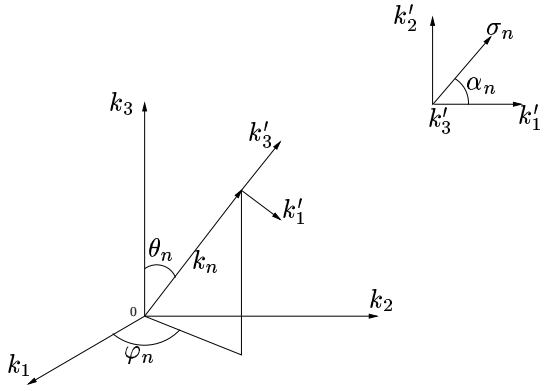

Fig. 1 Geometry for the n^{th} mode.

The vector $\mathbf{k}_n$ is chosen randomly on a sphere with radius k_n. This to ensure isotropy of the generated velocity field. By the assumption of incompressibility the continuity equation gives the following relation

$$
\mathbf{k}_n \cdot \sigma_n \equiv 0 \qquad \text{for all} \qquad n \tag{3}
$$

The wave number vector $\mathbf{k}_n$ and the spatial direction σ_n of the n^{th} mode are thus perpendicular. The angle α_n is a free parameter chosen randomly, see figure 1. The phase of each mode ψ_n is chosen with uniform probability between $0 \leq \psi_n \leq 2\pi$. The probability functions of all the random functions φ_n, ψ_n, θ_n and α_n are given in table 1.

$p(\varphi_n) = 1/(2\pi)$	$0 \leq \varphi_n \leq 2\pi$
$p(\psi_n) = 1/(2\pi)$	$0 \leq \psi_n \leq 2\pi$
$p(\theta_n) = (1/2)\sin(\theta)$	$0 \leq \theta_n \leq \pi$
$p(\alpha_n) = 1/(2\pi)$	$0 \leq \alpha_n \leq 2\pi$

Table 1 Probability distributions of random variables.

The probability function of θ, $p(\theta_n) = 1/2\sin(\theta)$ is chosen such that the distribution of the direction

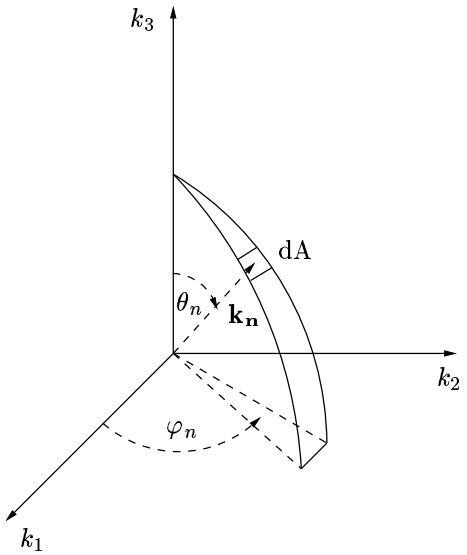

Fig. 2 The probability of a randomly selected direction of a wave in wave-space is the same for all dA **on the shell of a sphere.**

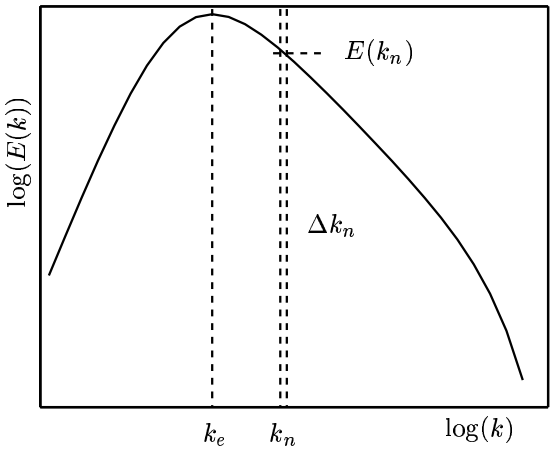

Fig. 3 von Kármán-Pao spectrum

of $\mathbf{k}_n$ is uniform on the surface of a sphere, see figure 2, i.e. the probability of a randomly selected direction is the same for all surface elements dA.

The amplitude $\hat{u}_n$ of each mode is computed so that the turbulence energy spectrum function $E(k_n)$ correspond to the energy spectrum for isotropic turbulence. This gives

$$\hat{u}_n = \sqrt{E(k_n)\Delta k_n} \tag{4}$$

where Δk_n is a small interval in the spectrum located at k_n, see figure 3. A model spectrum is used to simulate the shape of an energy spectrum for isotropic turbulence. In this way the sum of the squares of $\hat{u}_n$ over all n is equal to the total turbulence kinetic energy

$$\overline{k} = \sum_{n=1}^{N} \hat{u}_n^2 \tag{5}$$

The spectrum $E(k_n)$ is subdivided with a linear distribution as

$$k_n = k_1 + dk_l^{n-1} \quad \text{for} \quad n = 1, 2, \ldots, N \tag{6}$$

where

$$dk_l = \frac{(k_N - k_1)}{N-1} \tag{7}$$

It has been argued in previous studies[2] that a logarithmic distribution compared to a linear distribution results in a better resolution of the spectrum for low wave numbers corresponding to the most energy containing eddies. This is true but it has the side effect that the amplitudes of the highest wave numbers which then are poorly resolved are amplified by the increasing Δk_n for higher wave numbers in equation 4. A comparison of the energy distribution and the amplitude distribution for linear and logarithmic wave number distributions is presented in the result section. This comparison shows this effect and a linear distribution of the wave numbers is therefore used in this work.

The energy spectrum for isotropic turbulence is simulated by a von Kármán-Pao spectrum

$$E(k) = \alpha \frac{u'^2}{k_e} \frac{(k/k_e)^4}{[1+(k/k_e)^2]^{17/6}} e^{[-2(k/k_\eta)^2]} \tag{8}$$

where k is the wave number, $k_\eta = \varepsilon^{1/4}\nu^{-3/4}$ is the Kolmogorov wave number, ν is the molecular viscosity and ε is the dissipation rate. u'^2 is the r.m.s. value of the velocity fluctuations corresponding to the turbulent kinetic energy, $u'^2 = 2\overline{k}/3$. There are two free parameters in equation 8. The numerical constant α which determines the kinetic energy of the spectrum and the wave number k_e corresponding to the most energy containing eddies at the peak in the spectrum. The available information from the RANS solution is the turbulence kinetic energy $\overline{k}$ or, equivalently $3u'^2/2$, and the dissipation rate ε. These must be used in order to determine α and k_e and thereby the shape of the spectrum and the distribution of energy over different wave numbers. The numerical constant α can be determined by the requirement that the integral of the energy spectrum, equation 8, over all wave numbers should be equal to the total turbulent kinetic energy

$$\overline{k} = \int_0^\infty E(k)dk \tag{9}$$

Since equation 8 is derived for infinite Reynolds number α can be found independently of k_e by integrating equation 9 to get

$$\alpha = \frac{4}{\sqrt{\pi}} \frac{\Gamma(17/6)}{\Gamma(1/3)} \simeq 1.45276 \tag{10}$$

The turbulence length scale from the RANS solution is defined as

$$\Lambda = f_L c_\mu^{0.75} \frac{\overline{k}^{3/2}}{\varepsilon} \tag{11}$$

Assuming that the length scale from the RANS solution is the same as the integral length scale for isotropic turbulence gives the following relation

$$\Lambda = \frac{\pi}{2u'^2} \int_0^\infty \frac{E(k)}{k} dk \tag{12}$$

which is used to determine the wave number k_e corresponding to the most energetic length scales. The relation of k_e to Λ and α is

$$k_e = \frac{9\pi}{55} \frac{\alpha}{\Lambda} \tag{13}$$

where α is given in equation 10 and Λ is obtained from the RANS solution.

Time dependence and Convection – previous studies

In earlier studies, two methods have been developed to introduce time dependence in the synthesized velocity field.[1,2] The first method by Bechara *et al*[1] is based on independent generation of velocity fields $\mathbf{u}_t(\mathbf{x})$ (see equation 2) in every time step in the same manner as described above. The independent solutions are then filtered in time in every point to give a desired time correlation. The second method Bailly and Juvé[2] is based on introduction of time dependence in the actual generation by adding a time dependent term in the Fourier modes. The generated time dependent turbulent velocity $\mathbf{u}_t(\mathbf{x}, t)$ is then given by

$$\mathbf{u}_t(\mathbf{x}, t) = 2 \sum_{n=1}^{N} \hat{u}_n \cos(\mathbf{k}_n(\mathbf{x} - t\mathbf{u}_c) + \psi_n + \omega_n t)\sigma_n \tag{14}$$

In this expression $\mathbf{u}_c$ is the local convection velocity computed in the RANS solution, and ω_n is the angular frequency of the n^{th} generated mode. The angular frequency ω_n is a random function given by a Gaussian probability function

$$p(\omega_n) = \frac{1}{\overline{\omega}_n \sqrt{2\pi}} e^{(-(\omega_n - \overline{\omega}_n)^2 / 2\overline{\omega}_n^2)} \tag{15}$$

where $\overline{\omega}_n$ is the mean angular frequency of the n^{th} mode determined by $\overline{\omega}_n = u' k_n$, Bailly.[2]

The second method to introduce time dependence is attractive from computational point of view due to the difference in required computational effort and storage. In the first method a number of Fourier modes have to be generated in each time step. The resulting velocity fields need to be filtered a posteriori to get suitable statistical properties. This data need to be stored before it is used in the source terms in the linearized Euler computation, step (3). In the second method the velocity field can be generated for each time step independently and does not need to be filtered. It is then possible to include the generation of the turbulent velocity field in the solver. The only data that need to be stored in order to repeat a computation in this case are the random functions given in table 1. The first method is however attractive in the way that the time correlation can be chosen to follow a specified behavior. This is done through the filtering of the independent samples. This type of control is not possible in the second method. Also, choosing the relation between the angular frequency ω_n and the wave number k_n is somewhat arbitrary but at the same time an important parameter for the sound generation. The first method does not include any convection whereas the second does through the term $\mathbf{k}_n(\mathbf{x} - t\mathbf{u}_c)$ in the cosine argument.

Time dependence and Convection – present work

A way to retain the control of the time correlation and at the same time keep the required computational effort at a reasonable level is to introduce the time filter directly as the velocity field is generated. To include convectional effects a convection equation is solved for the filtered velocity field. The proposed method to introduce time dependence and convection is as follows. First define a realization of the generated turbulent velocity field as $\mathbf{u}_t^m(\mathbf{x})$ where superscript denotes time step m. Each generated field $\mathbf{u}_t^m(\mathbf{x})$ for all $1 < m < N$ is independent of the others and they have a zero statistical mean in time. In other words the generated velocity field is locally white noise. A new turbulent velocity field can then be computed via the equation

$$\mathbf{v}_t^m(\mathbf{x}) = a\mathbf{v}_t^{m-1}(\mathbf{x}) + b\mathbf{u}_t^m(\mathbf{x}) \tag{16}$$

where $a = \exp(-\Delta t/\tau)$ and $b = \sqrt{(1 - a^2)}$. τ is referred to as the time scale and defines the time separation for which the autocorrelation function is reduced to $\exp(-1)$. The expression for b ensures that the root mean square of $\mathbf{v}_t^m(\mathbf{x})$ is the same as for $\mathbf{u}_t^m(\mathbf{x})$. The time scale is computed from the RANS solution as

$$\tau = f_\tau \frac{\overline{k}}{\varepsilon} \tag{17}$$

where the factor f_τ is introduced for the possibility to modify the time scale.

To account for convection of the generated turbulent field $\mathbf{v}_t^m(\mathbf{x})$ a simple convection equation is solved for $\mathbf{v}_t^{m-1}(\mathbf{x})$

$$\frac{\partial(\overline{\rho}\mathbf{v}_t^{m-1})}{\partial t} + \frac{\partial(\overline{\rho u_j}\mathbf{v}_t^{m-1})}{\partial x_j} = 0 \qquad (18)$$

before it is used in equation 16. Absorbing boundary conditions based on characteristic variables are used when solving equation 18.

Using equation 16 to introduce time dependence as compared to equation 14 has the advantage of requiring a smaller number of modes. In equation 14 the velocity field is totally determined by each realization. A large number of modes is then required to accurately describe isotropic turbulence. In equation 16 the velocity field $\mathbf{v}_t^m(\mathbf{x})$ at a certain time is the weighted sum of all previous independent velocity fields $\mathbf{u}_t^m(\mathbf{x})$ each with different random parameters. Much fewer modes are then required to ensure accurate statistics. This property is shared with the first method described above.

The second method presented above has a disadvantage of loosing the space correlation cross a mean shear flow through the convective argument $\mathbf{k}_n(\mathbf{x} - t\mathbf{u}_c)$ in equation 14. This has been reported by Batten.[10] This de-correlation does not occur in the present method, as will be shown in the results.

Correlations of Generated Turbulence – Homogeneous Case

To see if the generated turbulent velocity field has the specified time and length scales, the autocorrelation and two-point correlations are computed from a generated homogeneous velocity field.

Using a first-order filter as in equation 16, the specified autocorrelation is an exponentially decaying function which in a discrete time separation is

$$\frac{\overline{\mathbf{v}_t^m \mathbf{v}_t^{m-p}}}{\overline{(\mathbf{v}_t^m)^2}} = a^p \qquad (19)$$

where p is the number of time steps separating $\mathbf{v}_t^m$ and $\mathbf{v}_t^{m-p}$ and the overline denotes an average over many realizations m. The specified and the computed autocorrelations are shown in figure 4.

The longitudinal two-point correlation $\overline{uu}(r,0,0)/\overline{uu}(0,0,0)$ is compared to the f-function for isotropic turbulence[11] and the transversal $\overline{vv}(r,0,0)/\overline{vv}(0,0,0)$ is compared to the g-function. The results are shown in figure 5. The correlations in time and space clearly follow the specified correlations.

3D Jet Simulation

The simulated jet is a Mach $M = 0.75$, Re $= DU_j/\nu = 750,000$ cold jet with a nozzle diameter of $D_j = 0.05$[m]. Jet flow conditions are shown in table 2.

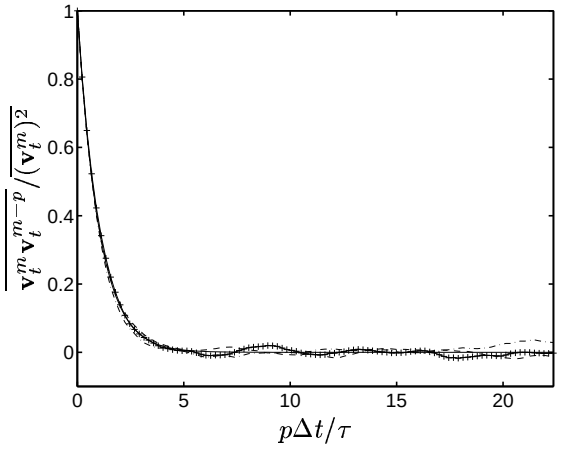

Fig. 4 Autocorrelation $\overline{\mathbf{v}_t^m \mathbf{v}_t^{m-p}}/\overline{(\mathbf{v}_t^m)^2}$ for generated turbulence as a function of normalized time separation $p\Delta t/\tau$. First-order filter in time. Solid line: analytical expression, equation 19; others: x_1, x_2, x_3 velocity autocorrelation.

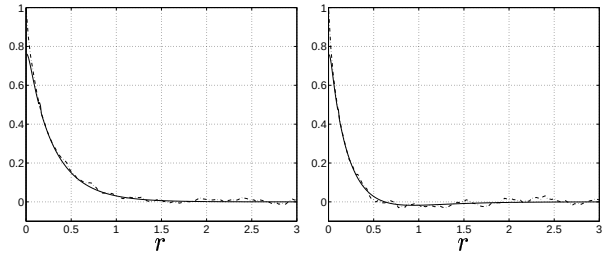

a) $\overline{uu}(r,0,0)/\overline{uu}(0,0,0)$ **b)** $\overline{vv}(r,0,0)/\overline{vv}(0,0,0)$

Fig. 5 Spatial two-point correlations. (a) longitudinal two-point correlation, (b) transversal two-point correlation. Solid lines: analytical expressions; dashed lines: from generated turbulent velocity fields.

Jet exit conditions		
Diameter, D_j	:	0.05 m
Mach number, M	:	0.75
Pressure, p_j	:	101.3 kPa
Temperature, T_j	:	288 K
Ambient conditions		
p_{amb}	:	101.3 kPa
T_{amb}	:	288 K

Table 2 Flow conditions

Source Region

The region in which the SNGR is applied is restricted to the region where the largest sources are expected. This region is a cylinder that starts from the nozzle and continues in the axial direction down to $x/D_j = 24$. Within this cylinder the source region is the set of cells where $\nu_t/\nu \geq 0.061$. This limit is chosen for numerical reasons to ensure that the Kolmogorov wave number is larger than the peak wave number k_e in the model von Kármán-Pao energy spectrum. This limit is quite arbitrary but convenient since the turbulence kinetic energy turns out to be very small where this value of ν_t/ν is reached.

Numerical Solver

The code for the linearized Euler equations is based on the finite volume method. The equations are discretized on a structured curv-linear non-orthogonal boundary-fitted multi-block mesh. The convective terms are discretized with a six point stencil. The coefficients of Tam's[12] fourth-order dispersion relation preserving finite difference scheme is converted to the equivalent finite volume coefficients. A fourth-order four step Runge-Kutta time marching technique is used for the time stepping. Artificial selective damping is used to prevent spurious waves from the boundaries and regions with stretching to contaminate the solution. The manner in which the artificial selective damping is introduced is described in Eriksson.[13]
The boundary conditions are based on local one dimensional analysis based on characteristic variables, Billson.[6]

A buffer layer is applied in the outflow region to attenuate vorticity and entropy disturbances before they reach the outflow boundary. The attenuation is done by adding a damping term to the governing equations in the outflow region of the computational domain, see Refs. (6, 14).

Computational setup

The block structure of the mesh is shown in figure 6. The spatial resolution is homogeneous $\Delta x/D_j = 0.1$ in the axial direction in the region $-7 \leq x/D_j \leq 29$. The resolution in the yz-plane is chosen so as to resolve the core of the jet and initial mixing layer with $\Delta y/D_j \approx 0.03$ with increased mesh size further away from the nozzle exit. The mesh support acoustic waves up to a frequency equivalent to Strouhal number $St = fD_j/U_j = 1.5$ with little dispersion and dissipation.

The buffer region is the part of the computational domain from $x/D_j = 29$ to the down-stream outflow at $x/D_j = 37$. Stretching of the mesh in the down-stream direction in the buffer layer has the additional effect that the artificial numerical dissipation at high wave numbers makes the buffer layer more efficient.

The time step is $\Delta t = 8.65 \times 10^{-7}$s equivalent to a maximum CFL-number based on spectral radius of $\mathrm{CFL} = 0.5$.

For the base-line simulation (see results section) the length and time scale factors used are $f_L = 1.0$ and $f_\tau = 1.0$. In the random field $N = 30$ modes are used and the lowest and highest wave numbers are $k_1 = 5$ and $k_N = 209$ corresponding to $k_1 = min(k_e)/5$ and $k_N = 2\pi/(6\Delta x)$ respectively.

A linear distribution of the energy spectrum (equation 8) is used in the present work as opposed to logarithmic in previous work.[1,2,8,9] When using a logarithmic distribution the amplitudes of modes at low wave numbers are suppressed and the amplitudes of modes at high wave numbers are emphasized due to the increasing Δk_n in equation 4 for higher wave numbers. Using a linear distribution gives a homogeneous distribution of the Δk_n.

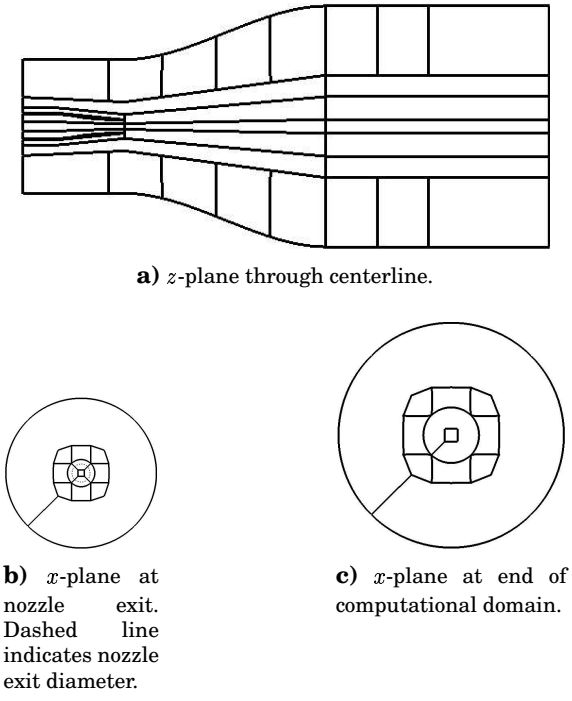

a) z-plane through centerline.

b) x-plane at nozzle exit. Dashed line indicates nozzle exit diameter.

c) x-plane at end of computational domain.

Fig. 6 Slices of the block structure of the linearized Euler mesh.

Figure 7 shows the energy distribution of the synthesized velocity fields for each mode for different down-stream positions in the center line (top) and in the jet shear layer (bottom). Figure 8 shows the amplitude of the same modes when computed with equation 4. A linear distribution is used to the left and a logarithmic to the right. The shift of the peak towards higher wave numbers between the energy and the amplitude in the logarithmic case is clear from figures 7 and 8. This shift in the peak is not present in the case with linear wave number distribution.

To validate the present method the far-field acoustic solution has been computed in two different ways, the Kirchhoff integral method[15] and the double time derivative formulation of the Lighthill acoustic analogy.[16] The Lighthill analogy solution is computed directly from the synthesized velocity field, see figure 9 whereas the Kirchhoff solution is based on the solution to the linearized Euler equations and thus including all steps in the present method.

Overall sound pressure levels (OASPL) and spectra of the acoustic data are compared with the LES of Andersson *et al*[5] and the measurements of the same flow by Jordan and Gervais.[4] The predicted acoustic data from the Kirchhoff integral method have been high-pass filtered to attenuate the effect of natural hydrodynamic instabilities in the linearized Euler equations. The Kirchhoff surface is placed five cells from the outer boundary of the

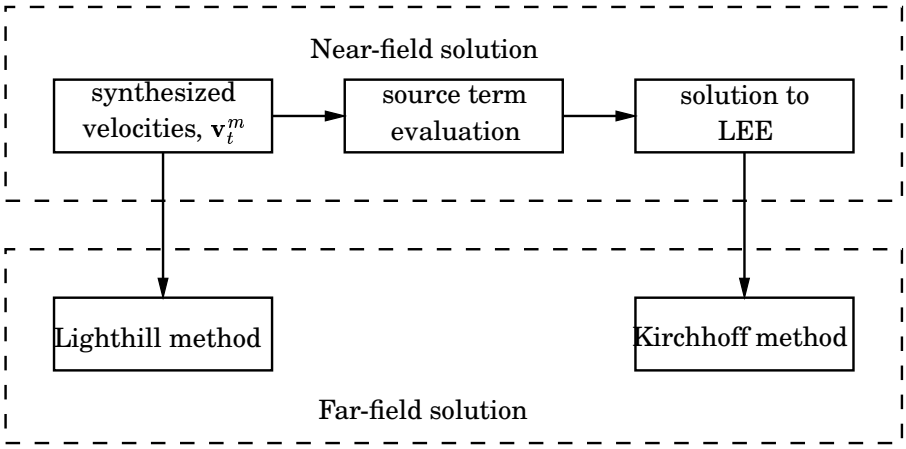

Fig. 9 Near-field to far-field solutions using Lighthill and Kirchhoff methods.

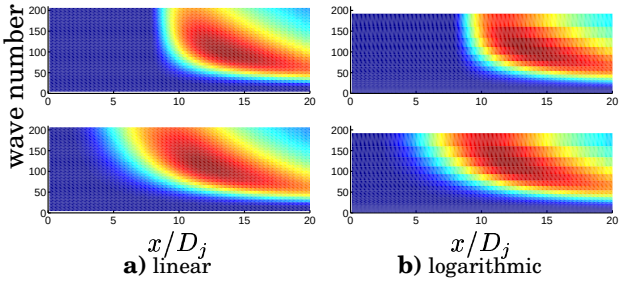

Fig. 7 Energy distribution

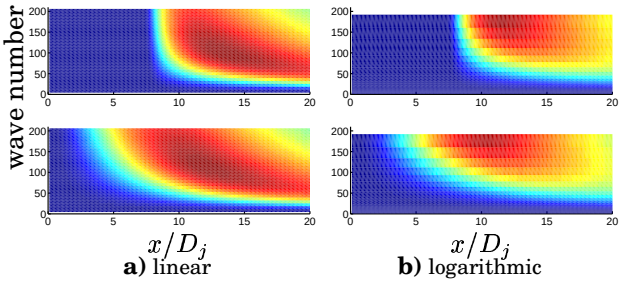

Fig. 8 Amplitude distribution

computational domain except in the outflow region where the surface is not closed over the turbulent region (see Ref. 17) and the Lighthill source region is chosen as the same region in space as the SNGR source region.

Choosing SNGR parameters

The SNGR parameters have been chosen in the following way. The near-field is calibrated using the length and time scale factors f_L and f_τ, see equations 11 and 17. The basis is that the near-field should be well calibrated before one can expect the solutions in the far-field to be in good agreement with measurements or the LES solutions. Thus the far-field pressure spectra and amplitude is determined by f_L and f_τ.

Results

The RANS solution which governs the statistic property of the proposed SNGR methodology has been validated against the LES data of Andersson *et al.*[5] and measurements, Jordan *et al.*[18] This is presented in Billson.[6]

Near-Field Results

Figure 10 shows the computed two-point space-time correlation function,

$$R_{1,1}(\mathbf{x},\phi,\tau) = \frac{\overline{u'(\mathbf{x},t)u'(\mathbf{x}+\phi,t+\tau)}}{\sqrt{\overline{u'^2(\mathbf{x},t)}}\sqrt{\overline{u'^2(\mathbf{x}+\phi,t+\tau)}}} \qquad (20)$$

where $\mathbf{x}$ and ϕ are the position and the space separation in x_1 direction respectively, overline $\overline{(.)}$ denotes time average and τ is time separation. In figure 10(a) the correlation is based on the LES data of Andersson *et al.*[5] and in figure 10(b) the correlation is based on the synthesized turbulent velocity field. Each curve represents the correlation in time of two points separated by a constant distance in space (axial direction). The envelope of the maxima of the correlation curves corresponds approximately[19] to the Lagrangian autocorrelation. The correlation for each space separation at zero time separation corresponds to the two-point space correlation and consequently the integral length scale.

Figure 11(a) shows the Lagrangian autocorrelation based on the space-time correlation for the LES data and the synthesized SNGR velocity field and figure 11(b) shows the two-point space correlation for the same sets of data. The correlations are in good agreement.

Since the spatial grid resolution is limited by the upper wave number constraint $k_N = 6\Delta x$, the kinetic energy of the synthesized velocity field will be lower than that of the RANS solution. The turbulence kinetic energy of the RANS solution, the resolved part (i.e. $k_1 \leq k \leq k_N$) of the energy spectrum (equation 3) and the synthesized turbulent velocity field in the shear layer are shown in figure 12. There is a large difference in the energy from the RANS solution compared with the resolved energy spectrum. This difference is due to the poor resolution in the x-direction which determines

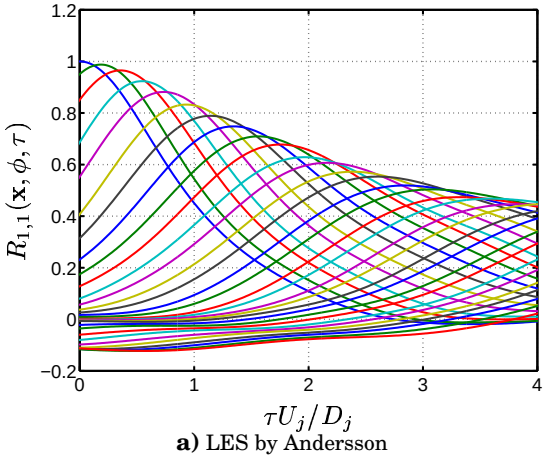

a) LES by Andersson

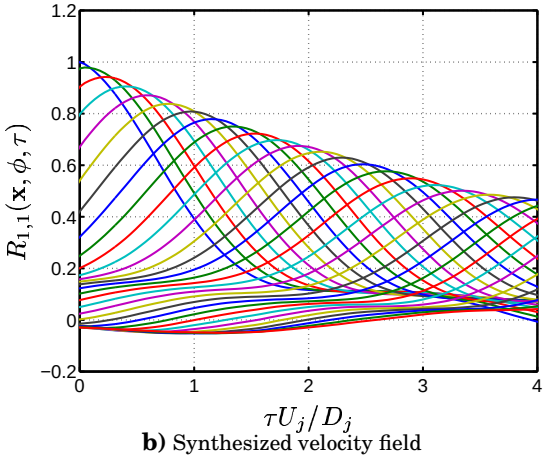

b) Synthesized velocity field

Fig. 10 Two-point space-time correlation (equation 20 in the axial direction at $(x/D_j, r/D_j) = (10, 0.5)$

the upper wave number, k_N, in the syntetisation. The energy which is lost is at small scales, see figure 13, and as such they are very compact as sound sources. The energy of the synthesized turbulence is however close to that of the resolved part of the energy spectrum which would be expected. A simulation where the convection operator has been turned off (see below) is also included in figure 12. Comparing the two curves for the simulations one can see that there is a small decrease in energy when the convection operator is used which is attributed to the fact that the time filter, equation 16, only has a limited time to feed the synthesized turbulence with new energy as the convection operator is transporting the velocity field down-stream.

The space and time correlations in figures 10 to 11 show good agreement between the LES and the synthesized velocity field. The turbulence kinetic energy levels in the simulations are lower than in the RANS solution, and this should have the effect of producing too low far-field sound levels. Even so, the proposed method to convect (equation 18) and filter (equation 16) the random velocity field (equation 2) can model the space-time statistics of an inhomogeneous turbulent velocity field.

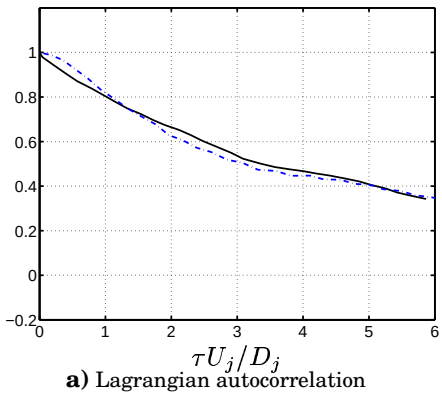

a) Lagrangian autocorrelation

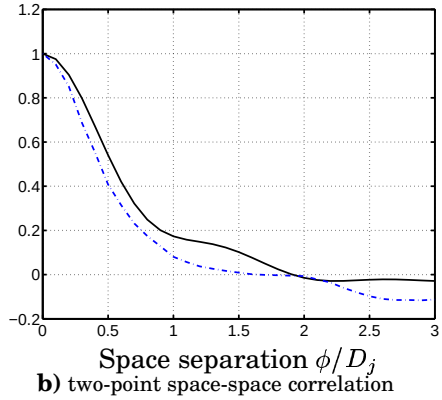

b) two-point space-space correlation

Fig. 11 Correlations at $(x/D_j, r/D_j) = (10, 0.5)$. Solid (black) line: synthesized velocity field, dash-dotted (blue) line: LES by Andersson

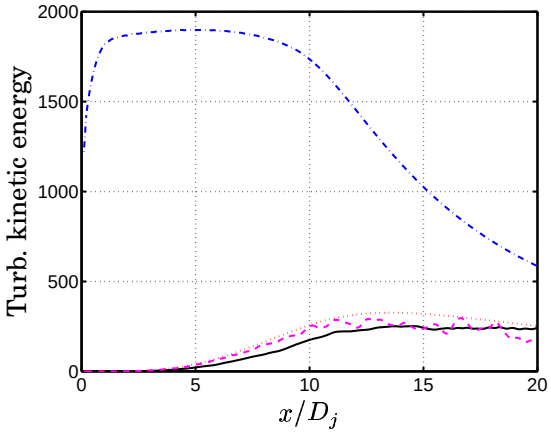

Fig. 12 Turbulence kinetic energy on a line in the axial direction at $r/D_j = 0.5$. Dash-dotted (blue) line: RANS; dotted (red) line: resolved spectrum (equation 8); solid (black) line: synthesized velocities (base-line case); dashed (magenta) line: synthesized velocities (no-convection case)

Far-Field Results

Due to growing hydrodynamic instabilities in the linearized Euler solution the far-field acoustic solution is high-pass filtered. This is done by applying a two-point Butterworth low-pass filter and subtracting the resulting signal. In this way, all low frequency information, below $St = 0.1$ is damped by the filter. Figure 14 shows time series of the unfiltered pressure disturbance, the low-pass filtered

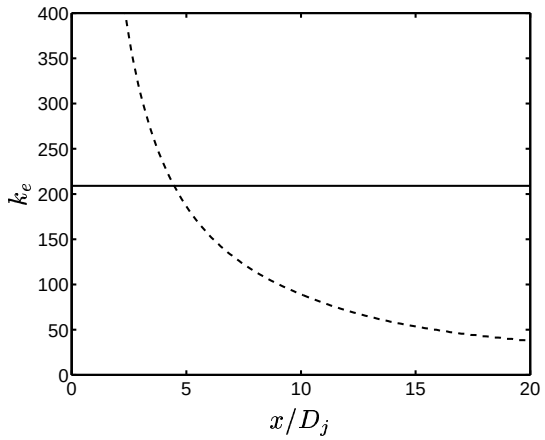

Fig. 13 Solid (black) line: highest synthesized wave $k_N = 209$; dashed (blue) line: peak wave number k_e in the shear layer, $r/D_j = 0.5$

and the resulting high-pass filtered signal.

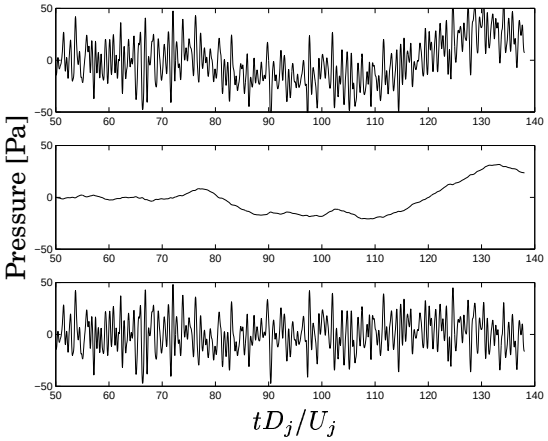

Fig. 14 Time series of pressure fluctuation at $(r/D_j, \theta) = (30, 30)$. Top: unfiltered; middle: low-pass filtered; bottom: high-pass filtered

In figure 15 the OASPL is computed at constant radius from the nozzle exit as a function of angle from the axial direction. Except for the offset of 10dB the directivity is the same for the measurements and the present method.

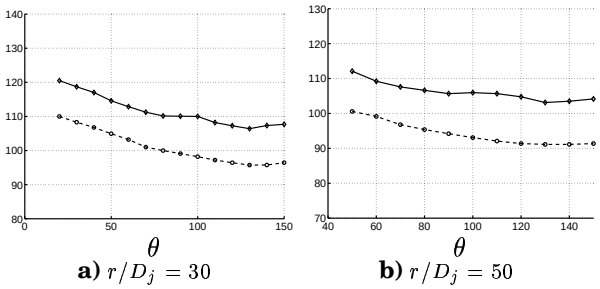

a) $r/D_j = 30$ **b)** $r/D_j = 50$

Fig. 15 OASPL (dB) at $r/D_j = 30$ and $r/D_j = 50$ for different angles θ from jet axis direction. Solid line (diamonds): present method (base-line case); dashed line (circles): measurements

The 1/3-octave band-pass filtered power spectrum of pressure from the observation point at $\theta = 30$ degrees in figure 15(a) is shown in figure 16. One can immediately see that there is a large difference in the frequency-content between the measurements and the simulation. The peak in the measured spectra is located at $St = 0.2$ as opposed to $St \approx 1.0 - 1.5$ in the simulation. Also as shown in figure 15 and evident in figure 16, the amplitude of the far-field signal is too high in the simulation. The OASPL is about 10dB larger than the measured data corresponding to a far-field pressure amplitude that is about 3 times over-estimated.

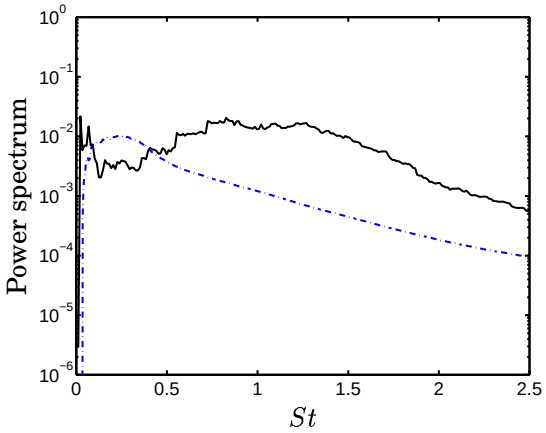

Fig. 16 1/3-octave power spectrum of pressure in an observation point at $(r/D_j, \theta) = (30, 30)$. Solid (black) line: present method (base-line case); dash-dotted (blue) line: measurements

Evaluation of Results

The near-field two-point statistics of the synthesized turbulence seems to be in good agreement with both measurements[3] and LES data.[5] This is shown in figures 10 and 11. The energy of the synthesized velocity field is however too low. Yet, the emitted far-field sound is over-predicted and has a different frequeny-content compared to the measurements. Possible sources for these inconsistent results in the present method has been classified as related to:

I The numerical issues in the computations

II The use of linearized Euler equations with source terms

III The synthesis of turbulence

The numerical issues account for numerical schemes, truncation of the source region and limited spatial and spectral resolution. In the second category one can include the use of the derived source terms for the linearized Euler equations, instabilities related to solving the linearized Euler equations in mean shear and the use of Kirchhoff's integral method. The third category involve, for example the spectral model of isentropic turbulence and the time filter (equation 16) and convection operator (equation 18).

The numerical issues in the computations

The numerical issues have been thoroughly tested and are well validated. The synthesized turbulence is well resolved with a shortest wave length of $\lambda_{min} = 6\Delta x$ for which the numerical scheme in the convection operator (equation 18) has little dispersion error. The numerical method used for the convection operator is the same as for the linearized Euler equations but with a four point stencil. The truncated source region would cause unwanted disturbances if the source term evaluation was performed all the way to the source region boundary. This is however avoided by evaluating the source terms only in the interior of the source region.

The use of linearized Euler equations with source terms

The far-field solution using the Lighthill analogy is computed using the synthesized velocity fields $\mathbf{v}_t^m(\mathbf{x})$, i.e. the modeled SNGR velocities, see figure 9. The Kirchhoff far-field solutions are computed from the solution of the linearized Euler equations using all the steps in the present methodology. If the far-field solution is the same for both the Lighthill analogy and the Kirchhoff integral method then the conclusion must be that the second category of possible reasons for inconsistent solutions above (the use of linearized Euler equations with source terms) can be ruled out.

Figure 17 shows the power spectrum of the far-field pressure computed using the Lighthill analogy and the Kirchhoff method. The far-field spectra are almost identical except for very low frequencies where there is presence of disturbances in the Kirchhoff method solution originating from hydrodynamic instabilities in the solution of the linearized Euler equations. The spectral peaks are located at the same place and the levels are the same in the two curves.

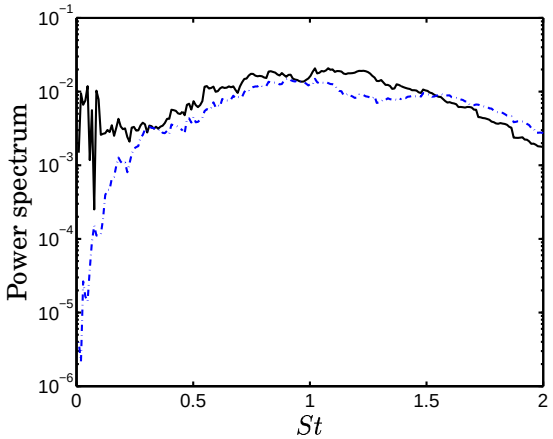

Fig. 17 $1/3$-octave power spectrum of pressure in an observation point at $(r/D_j, \theta) = (30, 30)$. Solid (black) line: Kirchhoff method; dash-dotted (blue) line: Lighthill's analogy

The conclusion is that the linearized Euler equations with source terms presented here indeed produce the correct sound field associated with a specified turbulent source field.

The synthesis of turbulence

There must be some feature in the synthesis of turbulence that gives the errors in the far-field. To investigate the reason for this, some parameters in the SNGR model were changed in order to investigate their impact on the near- and far-field solutions. The following parameters in the present SNGR method were investigated

- Length scale, f_L
- Time scale, f_τ
- Convection set to zero
- Divergence of source field
- Neglection of energy in wavespace

Length scale

Figure 18 shows the two-point space correlation $R_{1,1}(\mathbf{x}, \phi, 0)$ in the shear layer for two different values of the length scale parameter and the corresponding far-field power spectra of pressure are shown in figure 19. As can be seen in figures 18 and 19 the increasing length scale results in far-field spectra with increasing energy and also a shift in the peak in the spectral energy. The compactness of the source field is decreased with the increased length scale and through the source terms in equation 1, this changes the peak in the far-field spectra and the energy of the emitted sound.

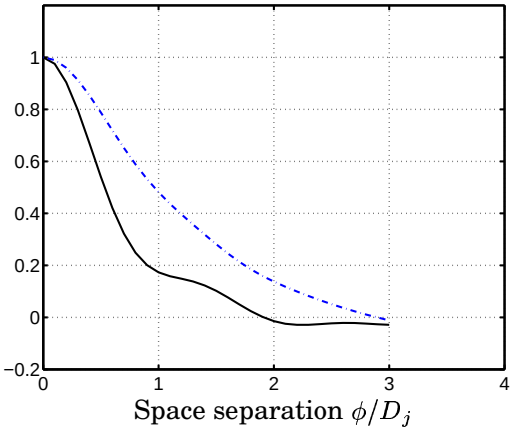

Fig. 18 Two-point space correlation located at $(x/D_j, r_j/D_j) = (10, 0.5)$. Solid (black) line: $f_L = 1$; dash-dotted (blue) line: $f_L = 6$

Time scale

Changing the factor for the time scale from $f_\tau = 1$ to $f_\tau = 6$ result in the autocorrelations in figure 20. The far-field power spectrum of pressure for the increased time scale case is included in figure 19. The effect of increasing the time scale of the source field clearly increases the amplitude of the emitted sound. However, contrary to what might

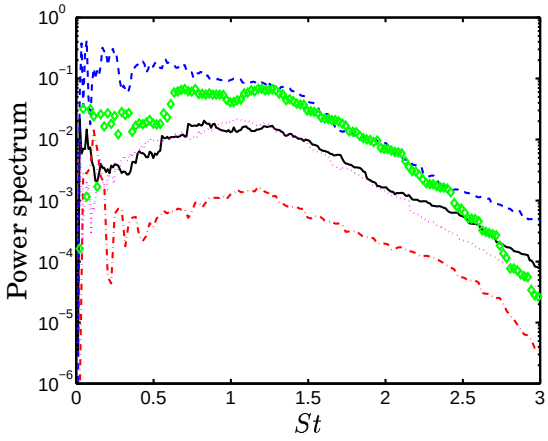

Fig. 19 Power spectrum of far-field pressure (1/3 octave band pass filtered. Solid (black): base-line case; dashed (blue): increased length scale; dash-dotted (red): increased time scale; dotted (magenta): no-convection case; diamonds (green): homogeneous source field

be expected, the location of the spectral peak is not drastically modified by the increased time scale. The time scale in the present SNGR model seems to primarily have an effect on the compactness of the source field but that the effect is the same for all scales and thus not changing the spectral peak in the far-field sound.

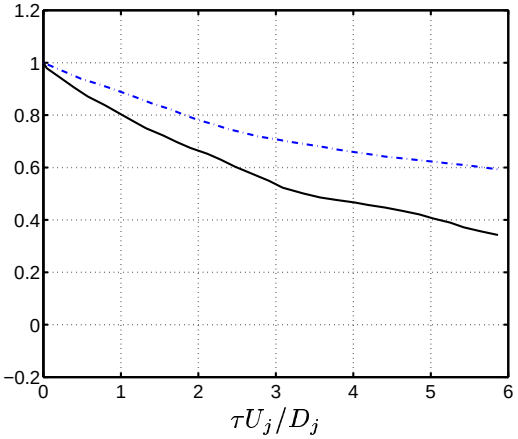

Fig. 20 Lagrangian autocorrelation (time correlation in the convected reference field). Solid (black) line: $f_\tau = 1$; dash-dotted (blue) line: $f_\tau = 6$

Convection set to zero

There was some concern that the convection operator (equation 18) would cause the same decorrelation that has been observed in the previously proposed method described above (equation 14), see Ref. (10). The time dependence and convectional operator is not the same in the present work however and the issue needs to be investigated. Figure 19 shows the far-field spectrum for a computation where the convection in the SNGR model has been turned off. The result is almost identical to the base-line case suggesting that the convection operator does not greatly change the nature of the emitted sound.

Divergence of source field

One of the assumptions made in the development of the SNGR method is that the isotropic turbulence is indeed isotropic. The homogeneity assumption implied in this is used to ensure that the resulting velocity fields are solenoidal and thus having a zero divergence. A velocity field that is not solenoidal will have a non-zero divergence which may be a source of sound when the velocity fields are used to evaluate the source terms. Some of the parameters in the SNGR model are evaluated locally (in space) from the RANS solution. These are the turbulence kinetic energy $\overline{k}$, the time scale τ and the length scale Λ of the synthesized turbulence. This local evaluation of SNGR parameters will introduce divergence and the role of this divergence as a source of sound must be investigated.

The divergence evaluated from the LES and the synthesized velocity field in the base-line case is shown in figure 21. Two differences between the synthesized velocities and the LES velocities are evident in figure 21. One is the difference in amplitude and the other is the shift in the peak region of the divergence. In the LES the divergence is most pronounced at $x \leq 5$, i.e. close to the end of the potential core whereas the divergence in the synthesized velocity field continues to grow downstream from this region.

The same property is shown in figures 22 and 23 for the case of no convection and also a case with a homogeneous source term field. The state of the source field in the homogeneous case was chosen to that in RANS solution at the spatial location $(x, r) = (5D_j, 0.5D_j)$, where the turbulence kinetic energy $\overline{k}$ is large. The divergence of the synthesized velocities in the no-convection case is clearly lower than in the base-line case. The convection operator in equation 18 does apparently introduce divergence in this inhomogeneous mean flow. The decrease in the divergence is even more evident in the homogeneous case in figure 23. This is expected since the homogeneous case satisfies the assumptions made for the flow to be solenoidal. The resulting far-field spectrum is plotted in figure 19 as the diamonds (green). The divergence introduced by not satisfying the assumptions for the flow to be solenoidal is clearly not the source of the inconsistent results between the near-field (figures 10 and 11) and the far-field (figures 15 and 16).

Neglection of energy in wavespace

The last parameter tested was the effect of the poor resolution in the axial direction on the energy content of the synthesized velocity field. It is clear from figure 12 that a large portion of the energy is neglected in the synthesized velocity field, especially in the beginnig of the shear layer where the length scales are smaller than further downstream.

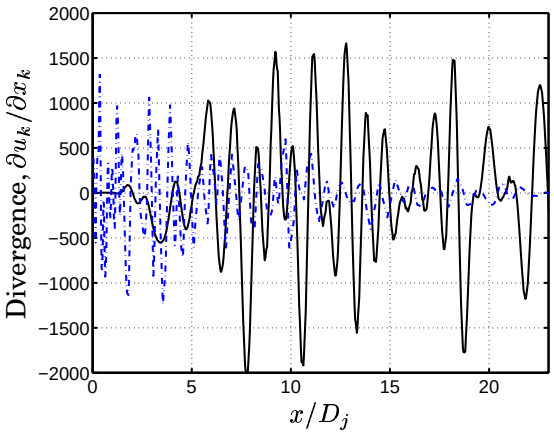

Fig. 21 Divergence of velocity evaluated on a line in the axial direction at a radius $r = 0.5D_j$. Solid (black): synthesized velocities (base-line case); dash-dotted (blue): LES by Andersson

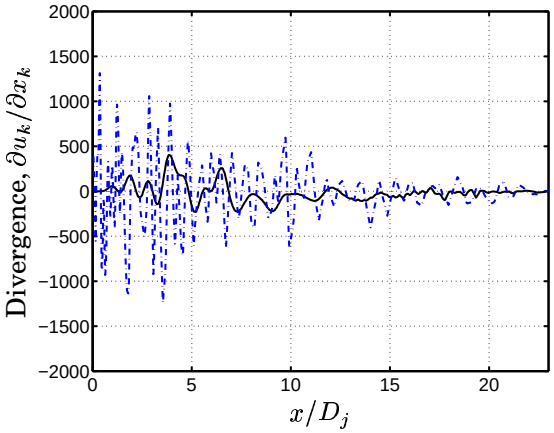

Fig. 22 Divergence of velocity evaluated on a line in the axial direction at a radius $r = 0.5D_j$. Solid (black): synthesized velocities (no-convection case); dash-dotted (blue): LES by Andersson

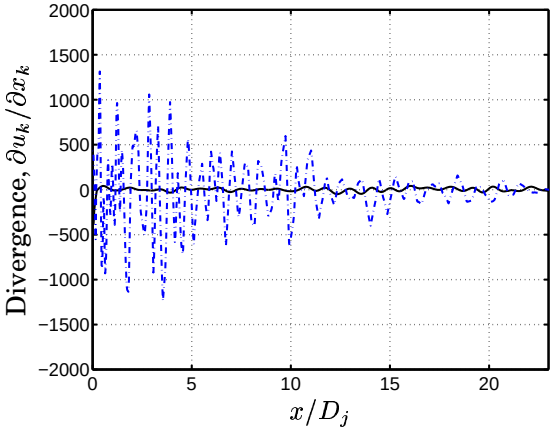

Fig. 23 Divergence of velocity evaluated on a line in the axial direction at a radius $r = 0.5D_j$. Solid (black): synthesized velocities (homogeneous case); dash-dotted (blue): LES by Andersson

The effect of truncating the spectrum at the high wave numbers is that the resulting two-point correlation and the length scale become too large. This can be seen in figure 24 showing the f-function (longitudinal two-point correlation coefficient) for isotropic turbulence (see Hinze[11]) based on the wavespace-truncated energy spectrum, i.e. the resolved part of the von Kármán-Pao spectrum and based on the same spectra but for all wave numbers.

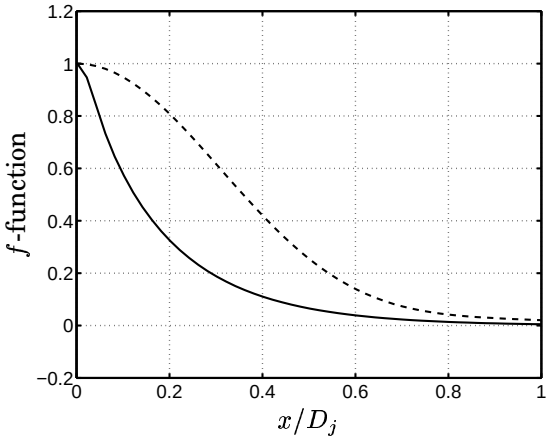

Fig. 24 f-function evaluated from the energy spectrum (equation 8) located at $(x/D_j, r/D_j) = (10, 0.5)$. Solid line: for all wave numbers; dashed line: for resolved wave numbers.

In the base-line case above the parameter f_L was calibrated such that the two-point correlation in figure 11(b) would match the LES data. In doing so, the value of the length scale parameter $f_L = 1.0$ was determined using a velocity field computed from a truncated spectrum. A length scale parameter of $f_L = 1.0$ is consequently calibrated to a too small value to compensate for the over-predicted two-point correlation resulting from the truncation of the energy at higher wave numbers.

The conclusion is that one should expect the two-point correlations from the synthesized velocity field to be larger than those of the LES data when a large portion of the energy at the high wave numbers has been omitted.

The effect of an increased length scale factor can be seen in figure 18 and figure 19 where the length scale factor was increased to $f_L = 6$ as compared to the base-line case. Increasing the length scale makes the synthesized turbulence less compact by moving the energy to the lower wave numbers. This also shifts the peak in the power spectrum of the far-field sound towards lower frequencies, see figure 19. The amplitude of the far-field sound is at the same time increased by the decreased compactness of the synthesized velocity field. Also the energy of the synthesized velocity field is increased due to a better resolution of the synthesized velocities.

By using $f_L = 6$ as in the length scale test above and at the same time lowering the amplitude in the time filter , i.e. $b = \sqrt{A(1-a^2)}$ in equation 16 using $A = 0.1$, the far-field solution shown in figures 25 and 26 is obtained. Observe that the calibration of the amplitude A was performed so that the OASPL would be in agreement with the measurements for $(r/D_j, \theta) = (30, 30)$. The far-field spectrum is in

quite good agreement with the measured data as well as the directivity which is within 4 dB from the measured OASPL.

The same arguments which were used for the length scale factor and the two-point correlations above can also be used for the time scale factor and the Lagrangian autocorrelation. It is thus likely that the time scale factor $f_\tau = 1$ is too small and should be increased to compensate for the truncation of turbulence at high wave numbers. The result in this case would be a decrease of the far-field sound as shown in the time scale test above, see figure 19.

A simulation using the present method with increased time- and length-scale factors would result in an improved jet noise prediction compared to the presented base-line case, without adjusting the amplitude A in the time filter. Due to time constraints this has not yet been performed.

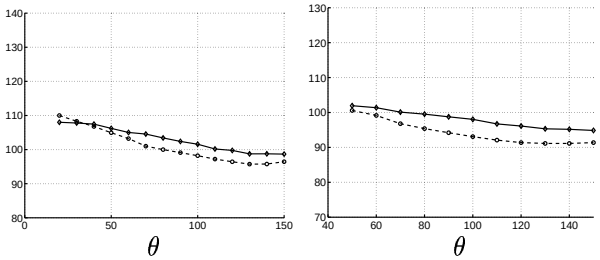

a) $r/D_j = 30$ **b)** $r/D_j = 50$

Fig. 25 OASPL at $x/D_j = 30$ and $x/D_j = 50$ for angles from jet axis direction. Solid line (diamonds): far-field calibrated simulation; dashed line (circles): measurements

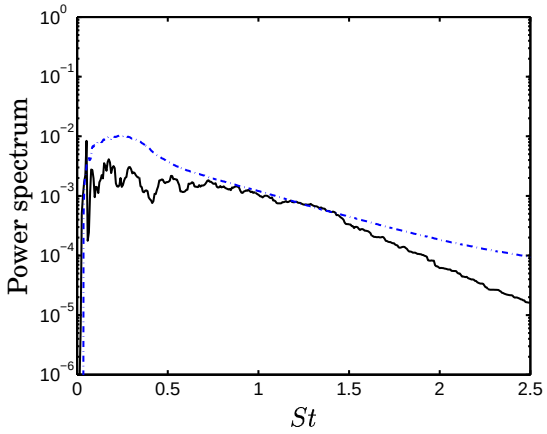

Fig. 26 Power spectrum of pressure in an observation point at $(r/D_j, \theta) = (30, 30)$. Solid line: far-field calibrated simulation; dashed line: measurements

Conclusions

A method has been presented in which a RANS solution of a jet is the basis of synthesized turbulence which in turn is used to evaluate source terms for the linearized Euler equations. The linearized Euler equations produce, when excited by the source terms, the acoustic field connected to the synthesized turbulence.

It is shown that the near-field statistics of a high Mach number jet can be simulated using the present method. Two-point statistics as space correlations and Lagrangian time correlations based on the synthesized turbulence are very close to those of the LES. The associated far-field solution does not agree well however, with those of the LES simulations or measurements. The directivity of the far-field sound is well predicted but the amplitude and spectral information differ from the measurements.

However, it is shown that the source terms to the linearized Euler equations do make the equations respond correctly to a given turbulent velocity field and that the equations govern the associated sound field. This confirms the results from Ref. (7).

It is further shown that the approach of calibrating the near-field synthesized velocity field to the LES solution will in fact cause the length scale and the time scale of the synthesized velocity field to be under-predicted. The reason for this lies in the limitations of the SNGR method connected to the spatial grid resolution.

A simulation using a modified length scale and amplitude is shown to agree well with measured far-field data. Amplitude, directivity and spectra are close to those of the measurements, but the generality of the method is unclear since a far-field calibration is the basis for the obtained results.

Acknowledgment

This work was conducted as part of NFFP (National Flight Research Program) as well as the EU 5th Framework Project JEAN (Jet Exhaust Aerodynamics & Noise), contract number G4RD-CT2000-000313. Computer time at the Sun-cluster, provided by UNICC at Chalmers, is gratefully acknowledged.

References

[1]Bechara, W., Bailly, C., Lafon, P., and Candel, S. M., "Stochastic Approach to Noise Modeling for Free Turbulent Flows," *AIAA Journal*, Vol. 32 , No. 3, 1994, pp. 455–463.

[2]Bailly, C. and Juvé, D., "A Stochastic Approach To Compute Subsonic Noise Using Linearized Euler's Equations," AIAA Paper 99-1872, 1999.

[3]P. Jordan and Y. Gervais, "Modelling self and shear noise mechanisms in anisotropic turbulence," The 9th AIAA/CEAS Aeroacoustic Conference, AIAA 2003-8743, Hilton Head, South Carolina, 2003.

[4]P. Jordan, Y. Gervais, J.-C. Valiére and H. Foulon, "Results from acoustic field measurements," Project deliverable D3.6, JEAN - EU 5th Framework Programme, G4RD-CT2000-00313, Laboratoire d'Etude Aerodynamiques, Poitiers, 2002.

[5]Andersson, N., Eriksson, L.-E., and Davidson, L., "Large–Eddy Simulation of a Mach 0.75 Jet," The 9th AIAA/CEAS Aeroacoustics Conference, AIAA 2003-3312, Hilton Head, South Carolina, 2003.

[6]Billson, M., "Computational Techniques for Jet Noise Predictions," *Lic. Thesis, Department of Thermo and Fluid Dynamics, Chalmers University of Technology, Gothenburg*, 2002.

[7]Billson, M., Eriksson, L.-E., and Davidson, L., "Acoustic Source Terms for the Linear Euler Equations on Conservative form," The 8th AIAA/CEAS Aeroacoustics Conference, AIAA 2002-2582, Breckenridge, Colorado, 2002.

[8]Kraichnan, R., "Diffusion by a random velocity field," *J. Comp. Physics*, Vol. 13(1), 1970, pp. 22–31.

[9]Karweit, M., Blanc-Benon, P., Juvé, D., and Comte-Bellot, G., "Simulation of the propagation of an acoustic wave through a turbulent velocity field: A study of phase variance," *J. Acoust. Soc. Am.*, Vol. 89(1), 1991, pp. 52–62.

[10]Batten, P., Goldberg, U., and Chakravarthy, S., "Reconstructed Sub-Grid Methods for Acoustics Predictions at all Reynolds Numbers," The 8th AIAA/CEAS Aeroacoustics Conference, AIAA 2002-2511, Breckenridge, Colorado, 2002.

[11]Hinze, J., *Turbulence, Second edition*, McGraw Hill, 1975.

[12]Tam, C. and Webb, J., "Dispersion-Relation-Preserving Finite Difference Schemes for Computational Acoustics," *J. Comp. Physics*, Vol. 107, 1993, pp. 262–281.

[13]Eriksson, L.-E., "Development and validation of highly modular flow solver versions in G2DFLOW and G3DFLOW," Internal report 9970-1162, Volvo Aero Corporation, Sweden, 1995.

[14]Colonius, T., Lele, S., and Moin, P., "Sound generation in a mixing layer," *Journal of Fluid Mechanics*, Vol. 330, 1997, pp. 375 – 409.

[15]Lyrintzis, A. S., "Review: The use of Kirchhoff's method in computational aeroacoustics," *ASME: Journal of Fluids Engineering*, Vol. 116, 1994, pp. 665 – 676.

[16]Crighton, D., "Basic Principles of Aerodynamic Noise Generation," *Progress in Aerospace Sciences*, Vol. 16 No. 1, 1975, pp. 31–96.

[17]Freund, J. B., Lele, S. K., and Moin, P., "Calculation of the Radiated Sound Field Using An Open Kirchhoff Surface," *AIAA Journal*, Vol. 34 No. 5, 1996, pp. 909 – 916.

[18]P. Jordan, Y. Gervais, J.-C. Valiére and H. Foulon, "Final results from single point measurements," Project deliverable D3.4, JEAN - EU 5th Framework Programme, G4RD-CT2000-00313, Laboratoire d'Etude Aeródynamiques, Poitiers, 2002.

[19]M. J. Fisher and P. O. A. L. Davies, "Correlation measurements in a non-frozen pattern of turbulence," *Journal of Fluid Mechanics*, Vol. 18, 1963, pp. 97–116.